Structure and Temperature Behavior of Metallo-supramolecular Assemblies

Y. Bodenthin,*,† U. Pietsch,† J. Grenzer,†,# Th. Geue,†,⊥ H. Möhwald,‡ and D. G. Kurth*,‡,§

University Potsdam, Department of Physics, P.O. Box 601553, D-14415 Potsdam, Germany, Max Planck Institute of Colloids and Interfaces, D-14424 Potsdam, Germany, and National Institute for Materials Science, 1-1 Namiki, Tsukuba, Ibaraki 305-0044, Japan

A detailed structural analysis of a Langmuir–Blodgett (LB) multilayer composed of a polyelectrolyte–amphiphile complex (PAC) is presented. The PAC is self-assembled from metal ions, ditopic bis-terpyridines, and amphiphiles. The vertical structure of the LB multilayer is investigated by X-ray reflectometry. The multilayer has a periodicity of 57 Å, which corresponds to an architecture of flat lying metallo-supramolecular coordination polyelectrolyte (MEPE) rods and upright-standing amphiphiles (dihexadecyl phosphate, DHP). In-plane diffraction reveals hexagonal packing of the DHP molecules. Using extended X-ray absorption fine structure (EXAFS) experiments, we prove that the central metal ion is coordinated to the terpyridine moieties in a pseudo-octahedral coordination environment. The Fe–N bond distances are 1.82 and 2.0 Å, respectively. Temperature resolved measurements indicate a reversible phase transition in a temperature range up to 55 °C. EXAFS measurements indicate a lengthening of the average Fe–N bond distance from 1.91 to 1.95 Å. The widening of the coordination cage upon heating is expected to lower the ligand field stabilization, thus giving rise to spin transitions in these composite materials.

Introduction

Metallo-supramolecular modules (MEMOs) generated from metal ion directed self-assembly of organic ligands are promising components for the construction of nanotechnological devices because they possess a wide range of photochemical, electrochemical, reactive, and kinetic properties.[1–3] The non-covalent character of the metal ion ligand interaction can be explored for adaptive and responsive materials. The occurrence of semioccupied d-orbitals gives rise to interesting electronic and magnetic properties including strong absorption, high quantum yields, suitable excited state lifetimes, luminescence, and tunable redox states. These features can be explored for optical nonlinearity[4] or photomediated charge separation.[5] The splitting of the d-orbitals in a ligand field of appropriate symmetry and strength can give rise to heat-induced or photoinduced spin transition and spin crossover phenomena, the most intriguing one being light-induced excited spin state trapping (LIESST),[6] reverse[7] and low spin LIESST.[8] However, the progress in designing increasingly complex architectures through metal-ion-induced self-assembly has not been matched by corresponding developments in implementing the active functional units in material structures, such as nanostructures, thin films or mesophases. Typically, the final metallo-supramolecular assembly is isolated as crystalline solid, which is hard to process in suitable device architectures. Using a colloid chemical approach based on amphiphilic self-assembly, we developed an approach to tailor the physicochemical properties of metallo-supramolecular assemblies including solubility, phase behavior, and processability. The metallo-supramolecular assemblies of interest are assembled from ditopic terpyridine ligands and suitable metal ions, which results in linear metallo-supramolecular coordination polyelectrolytes (MEPEs). Due to the positive charge, MEPEs spontaneously assemble with amphiphilic molecules, giving rise to the corresponding polyelectrolyte–amphiphile complex (PAC) (Scheme 1). The hydrophobic, neutral assembly is soluble in apolar organic solvents and forms perfectly straight nanostructures,[9] monolayers at the air–water interface, and liquid crystalline phases.[10] The Langmuir monolayers can be transferred onto solid supports by means of the Langmuir–Blodgett technique. The resulting, highly ordered Langmuir–Blodgett (LB) films are ideal model systems to study structure–property relationships in periodic two-dimensional arrangements of metal ions. Recently, we found that Fe^{2+}–MEPE exhibits a paramagnetic response at room temperature.[11] To understand the origin of this untypical phenomenon for Fe^{2+} bis-terpyridine complexes, we present a detailed temperature-dependent investigation of the LB film structure at the mesoscopic and molecular length scale using synchrotron-based experiments.

Experimental Section

Materials. The compounds were prepared according to literature procedures.[12]

Sample Preparation. Langmuir monolayers and Langmuir–Blodgett multilayers were prepared according to procedures published.[13] The LB transfer was carried out with a NIMA film balance (Hellma Optik, Forest Hills, NY). We used silicon wafers (Wacker AG, Munich) as substrates, which were cleaned according to the KERN procedure.[14] Monolayer transfer was carried out at 20 °C, at a constant surface pressure of 40 mN/m and a dipping speed of 6 mm/min. The transfer ratios were always 0.95 ± 0.05 for up- and downstroke deposition.

* To whom correspondence should be addressed. E-mail: bodenth@rz.uni-potsdam.de (Y.B.); kurth@mpikg-golm.mpg.de (D.G.K.).
† University Potsdam.
Present address: Research Center Rossendorf, Department of Structural Diagnostics, P.O. Box 510119, D-01314 Dresden, Germany.
⊥ Present address: Laboratory for Neutron Scattering, ETH Zurich & Paul Scherrer Institute, CH-5232 Villigen PSI, Switzerland.
‡ Max Planck Institute of Colloids and Interfaces.
§ National Institute for Materials Science.

SCHEME 1: Self-Assemblies of Ditopic Bis-terpyridine Ligands, Transition Metal Ions, and Amphiphiles Results in Metallo-supramolecular Coordination Polyelectrolytes (MEPEs) and the Corresponding Polyelectrolyte−Amphiphile Complexes (PACs)[a]
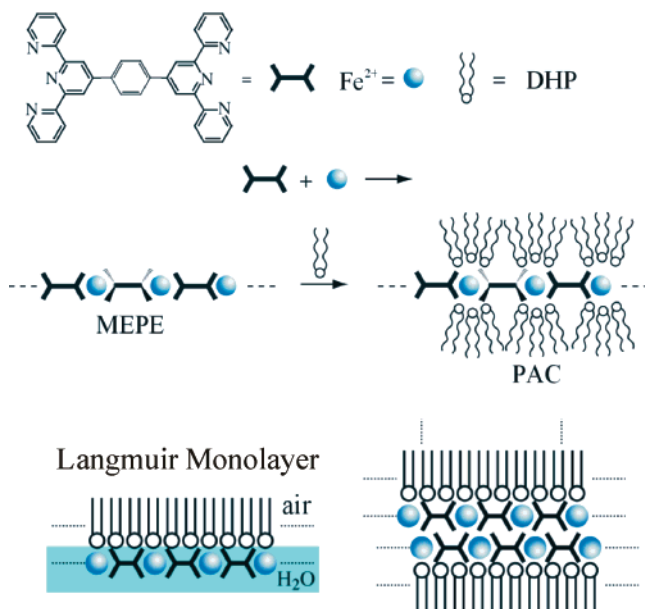
[a] Thin films of PAC were prepared by means of the Langmuir−Blodgett technique.

Measurements. X-ray reflectivity measurements were performed with a θ−2θ diffractometer (Stoe & Cie) using Cu Kα radiation with a wavelength of $\lambda = 1.54$ Å. The calculation of the reflectivity is performed using the Parrat formalism.[15] The vertical momentum transfer is defined as $q_z = 2\pi/\lambda \sin 2\alpha_i$, and the in-plane component, as $q_{x,y} = 2\pi/\lambda \sin 2\theta$ with the angle of incidence α_i and the in-plane scattering angle θ, respectively. Grazing incidence diffraction (GID) measurements were carried out at the D4 beam line at Hasylab using an angular-dispersive triple axis diffractometer and a wavelength of $\lambda = 1.24$ Å. Temperature-dependent specular reflection and grazing incidence diffraction measurements were carried out with the energy-dispersive reflectometer (EDR) at BESSY II using the experimental realization described in ref 16. Reflectance and diffraction data of a film were recorded at a given temperature using two energy-dispersive (ED) detectors. First, the reflectance data were recorded at an angle of incidence of 1° after which the angle of incidence was changed to 0.2° to collect the diffraction data. All other experimental parameters were kept constant. Therefore, reflectance and diffraction data probe the same structure of the film at that temperature. The recording time for each spectrum was 60 s. Extended X-ray absorption fine structure (EXAFS) experiments were undertaken at the KMC 2 beam line at BESSY II, using the fluorescence yield $I_{fluo}(E) \sim \mu(E)$ of the Fe^{2+} ions, where $\mu(E)$ represents the absorption.[17] To increase the signal, we used grazing incidence conditions ($\alpha_i = 0.15$−$0.2°$). The detector was attached perpendicular to the sample surface. To explore the data, we used a simplex fitting algorithm minimizing the residual $S = [\Sigma(\chi_{exp}(k) - \chi_{sim}(k))^2/\Sigma\chi_{exp}^2(k)]^{0.5}$. χ_{sim} was calculated using the standard EXAFS formula $\chi_{sim} = \Sigma_i (N_i/kr_i^2) \exp(-2\sigma_i^2 k^2) \exp[-2r_i/\lambda(k)] \times |f_i(k,r_i)| \sin[2kr_i + \Phi(k,r_i)]$. k represents the reduced wavenumber $k = \hbar^{-1}[2m_e(E - E_0)]^{0.5}$, E the photon energy, E_0 the iron absorption edge, N_i the occupation number, σ^2 the Debye−Waller factor, and r_i the radius of the shell. The
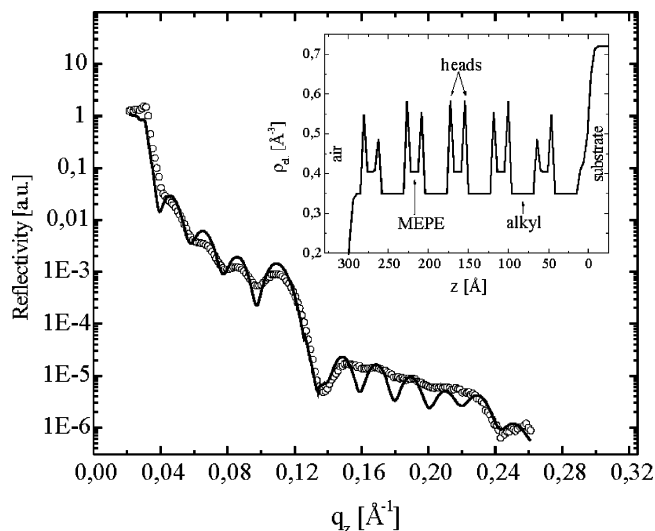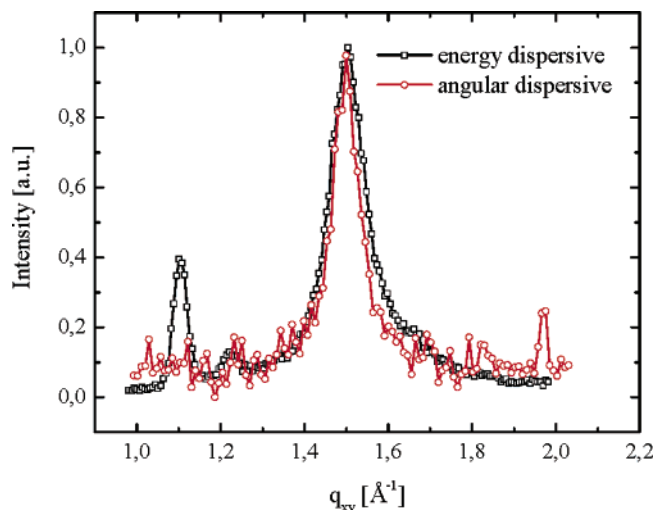

Figure 1. Measured reflectivity and theoretical calculation versus q_z of a film consisting of 11 monolayers. The Bragg peaks correspond to double layer distances with $d = 57 \pm 2$ Å and the Kiessig fringes to a total film thickness of $D = 311 \pm 3$ Å. The inset shows the resulting electron density profile. The zero position marks the film−air interface.

amplitude $f(k,r)$ and phase $\Phi(k,r)$ were calculated with the ab initio FEFF6 calculation. To avoid the "multiple solution trap",[18] the Fe−N distances were restrained to vary in an interval of ± 0.2 Å. The shift of the energy threshold ΔE_0 remains constant at $\Delta E_0 = -4.3$ eV for all fits. The simultaneously collected near-edge spectra (XANES) give no hint for other oxidation states of the iron.

Results

Vertical Structure. To determine the multilayer structure in the direction normal to the silicon surface, we use X-ray reflectometry. As a representative example, we present and discuss the reflectance data of the LB multilayer with 11 monolayers. Figure 1 shows the measured and computed reflectivity as a function of the vertical momentum transfer q_z. The occurrence of Kiessig fringes and Bragg peaks indicates a homogeneous film with an internal structure. The first- and second-order Bragg peaks at $q_z = 0.110 \pm 5 \times 10^{-3}$ Å^{-1} and $q_z = 0.220 \pm 5 \times 10^{-3}$ Å^{-1}, respectively, indicate an internal layering with a spacing of $d = 57 \pm 2$ Å. The Kiessig fringes with $\Delta q_z = 0.0202 \pm 1 \times 10^{-4}$ Å^{-1} correspond to a total film thickness of $D = 311 \pm 3$ Å. In the present case, the total thickness D is not an even multiple of the internal spacing d because an odd number of monolayers were transferred. Therefore, the maxima of the two sets of interfering fringes, one originating from the total thickness and the other from the internal layering, do not occur at the same q-position. As a result, we observe distorted Bragg peaks.

To retrieve a detailed picture of the internal structure, the reflectivity is modeled using a stratified stack of layers, each with a distinct electron density ρ and interface roughness δ. The inset in Figure 1 shows the computed electron density profile, which produces the best fit of the reflectivity data. The silicon interface is chosen as $z = 0$. The first box corresponds to a MEPE with a thickness of $d_{MEPE} = 7.3 \pm 0.8$ Å; the internal layer roughness is estimated to be $\sigma_{MEPE} = 1.5 \pm 0.5$ Å and the electron density to be $\rho_{MEPE} = 0.38 \pm 0.02$ Å^{-3}. The following box contains the phosphate heads groups of the amphiphilic molecules (dihexadecyl phosphate, DHP) with a thickness of $d_{head} = 3.0 \pm 0.5$ Å, a roughness of $\sigma_{head} = 1.0 \pm 0.5$ Å, and an electron density of $\rho_{head} = 0.56 \pm 0.03$ Å^{-3}.

Metallo-supramolecular Assemblies

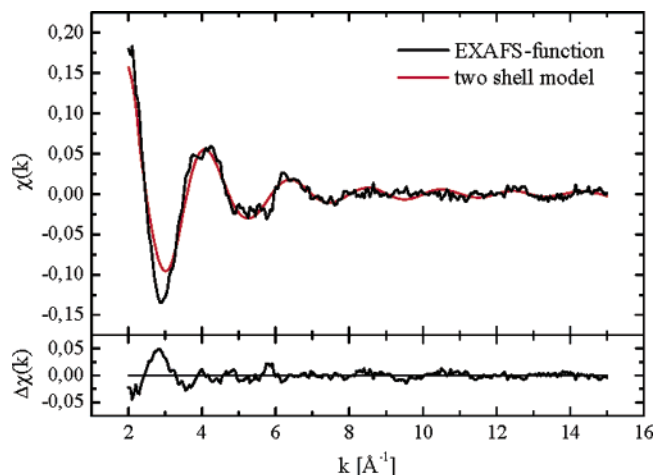*J. Phys. Chem. B, Vol. 109, No. 26, 2005* **12797**

Figure 2. Energy- (black) and angular-dispersive (red) in-plane diffraction data of a film consisting of 11 monolayers. The Bragg peak at $q_{x,y} = 1.5 \pm 0.2$ Å^{-1} corresponds to a hexagonal lattice arrangement of the DHP molecules with $d_{in} = 4.2 \pm 0.5$ Å. The peak at $q_{x,y} = 1.1$ Å^{-1} in the energy-dispersive recorded spectra reflects the K-fluorescence of the Fe^{2+} ions at $E = 6.4$ keV.

Figure 3. Representative EXAFS function $\chi(k) = (\mu(k) - \mu_0(k))/\mu_0(k)$ of Fe−PAC films. k represents the reduced wavenumber $k = \hbar^{-1}[2m_e(E - E_0)]^{0.5}$. The theoretical calculation of $\chi(k)$ results in two different Fe−N distances of $r_1 = 1.821 \pm 2 \times 10^{-3}$ Å and $r_2 = 1.999 \pm 2 \times 10^{-3}$ Å and occupation numbers of 2 and 4, respectively.

Finally, the third box is ascribed to the alkyl chains of DHP with a thickness of $d_{alkyl} = 17 \pm 1$ Å, a roughness of $\sigma_{alkyl} = 5 \pm 1$ Å, and an electron density of $\rho_{chain} = 0.33 \pm 0.02$ Å^{-3}. The same values are used for all strata constituting the multilayer. The determined parameters of this model are in good agreement with the values for the neat compounds: the electron densities are estimated to be $\rho_{MEPE} = 0.32$ Å^{-3}, $\rho_{head} = 0.53$ Å^{-3}, and $\rho_{alkyl} = 0.33$ Å^{-3}, respectively. Using molecular modeling, the width of the ligand is determined to be approximately 12 Å, and therefore, the average height of a flat lying MEPE chain is estimated to be 8−9 Å. The size of the phosphate group is determined to be approximately 3 Å, and the length of the alkyl chain in an all-trans conformation is approximately 19 Å. Apparently, the film consists of alternating strata of all-trans, upright-standing DHP molecules, and flat lying MEPE chains.

The correlation length of coherent scattering within the films is given by $\xi = 2\pi/\omega(q)$; ξ describes mainly the correlation length in the direction of the surface normal; $\omega(q)$ is the full width at half-maximum (FWHM) of the Bragg peaks and is estimated from the experimental data. For the 11 ML film, we estimate a correlation length of $\xi_{11ML} = 307 \pm 3$ Å. This value agrees fairly well with the thickness $D_{11ML} = 311 \pm 3$ Å. The correlation lengths and thicknesses for the other multilayers are $\xi_{1ML} = 24 \pm 1$ Å and $D_{1ML} = 26 \pm 1$ Å for 1 ML, $\xi_{5ML} = 137 \pm 2$ Å and $D_{5ML} = 132 \pm 2$ Å for 5 ML, and $\xi_{15ML} = 381 \pm 3$ Å and $D_{15ML} = 418 \pm 3$ Å for 15 ML. The stratification extends over approximately 12 layers beyond which the correlation of strata levels off due to the accumulation of defects with increasing layer numbers.

In-Plane Structure. The in-plane structure is revealed by grazing incidence diffraction (GID). Generally, the diffracted intensity is measured by angular-dispersive (AD) detection. This scheme is readily available and can provide high resolution data. In comparison to AD detection, energy-dispersive (ED) detection provides both diffraction and fluorescence data. In addition, the high temporal resolution (recording times of 60 s per spectra) allows temperature and time-dependent studies. Therefore, this method is ideally suited to study soft matter, where a high spectral resolution is not needed. To verify the quantitative agreement of the two detection schemes, we present results from both ED and AD detection. Figure 2 shows representative in-plane diffraction data for the PAC film with 11 monolayers measured with both methods.

In each case, the probe beam strikes the sample surface at an angle of incidence of $\alpha_i = 0.2°$. The beam is diffracted at in-plane lattice planes created by the lateral arrangement of DHP molecules. The diffraction peak at $q_{x,y} = 1.5 \pm 0.2$ Å^{-1} corresponds to a lattice spacing of $d_{in} = 4.2 \pm 0.5$ Å, which is in good agreement with values of LB films of fatty acid salts[19] and PAC films at the air−water interface.[20] The absence of a second-order peak indicates a hexagonal arrangement of the DHP molecules. The peak width $\omega(q_{x,y})$ is associated with the correlation length L of the lateral order of the molecules.[21] After correction of the experimental broadening, the correlation length is estimated to be $L_{ED} = 64 \pm 2$ Å and $L_{AD} = 75 \pm 2$ Å. This length scale corresponds to crystalline subdomains of about 15−18 neighboring DHP molecules.[22] The energy-dispersive spectra also show a second, smaller peak at $q_{x,y} = 1.1$ Å^{-1}, which is associated with the K-fluorescence of the Fe^{2+} ions at $E = 6.4$ keV.[23]

Structure of the Fe^{2+} Coordination Center. We employ X-ray absorption experiments (EXAFS) at the iron K-absorption edge to determine the next-neighbor coordination geometry around the central Fe^{2+} ions in the assembly. Figure 3 shows a representative EXAFS function, $\chi_{exp}(k) = (\mu(k) - \mu_0(k))/\mu_0(k)$, of the PAC multilayer with 11 monolayers. Also shown is the best fit which is obtained in terms of a two-core approximation with two different Fe−N distances, $r_1 = 1.821 \pm 2 \times 10^{-3}$ Å and $r_2 = 1.999 \pm 2 \times 10^{-3}$ Å, and occupation numbers of 2 and 4, respectively. These numbers define a deformed octahedron with the iron in the central position. The values correspond fairly well with average Fe−N next-neighbor distances found in the single crystal structure of the mononuclear bis-terpy Fe^{2+} complex with 1.885 Å for the Fe−N$_{central}$ distance and 1.981 Å for the Fe−N$_{terminal}$ distance.[24] Finally, it should be noted that it is not possible to obtain a satisfactory fit with a single shell model, where all bond distances are equal (not shown).

Temperature-Induced Structural Changes. As mentioned above, the time resolution with ED detection allows the determination of structural changes as a function of temperature. Figure 4 summarizes the changes of the integrated intensities of the Bragg peaks and diffraction peaks as well as the average Fe−N bond distances, $\langle r \rangle = (r_1 + r_2)/2$, as a function of
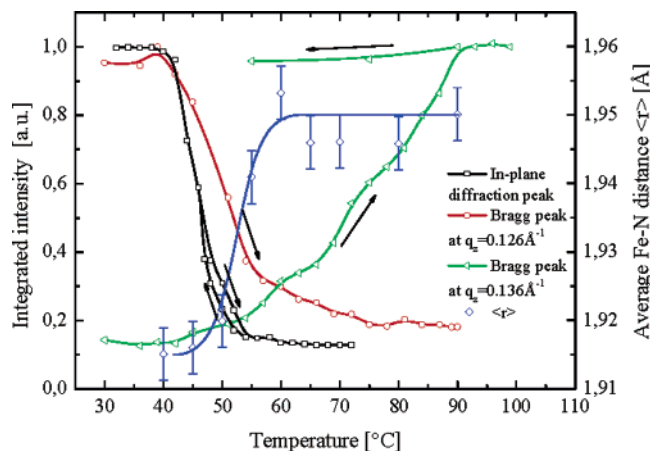
Figure 4. Thermal behavior of Fe−PAC films summarized in a typical phase plot. Here, integrated intensities of the Bragg peaks and diffraction peaks as well as the average Fe−N bond distances are plotted as a function of temperature. The decrease of the in-plane signal and the Bragg peak signal at $q_z = 0.126$ Å^{-1} indicates a reversible phase transition. The second irreversible phase transition above 55 °C (Bragg peak signal at $q_z = 0.136$ Å^{-1}) is associated with the loss of the out-of-plane and in-plane correlation. Additionally, the temperature-dependent average $\langle r \rangle = (r_1 + r_2)/2$ known from EXAFS measurements is plotted. It can be seen that a change in the film structure results in a change of the next-neighborhood of the iron ions.

temperature. The red trace corresponds to the first-order Bragg peak at $q_z = 0.11$ Å^{-1} ($d = 57$ Å). The intensity decreases rapidly as the film is heated from room temperature to approximately 55 °C. In this temperature range, the position of this peak shifts to $q_z = 0.126 \pm 5 \times 10^{-3}$ Å^{-1} (data not shown), which corresponds to a layer spacing of $d = 50 \pm 2$ Å. After cooling to room temperature, the layer spacing is $d = 52 \pm 2$ Å. During further heating and cooling cycles, the layer spacing changes reversibly between these two values. The contrast of the Kiessig fringes decreases during the first heating and is not completely recovered upon cooling. Additionally, the integrated intensity of the in-plane diffraction peak (black trace) decreases rapidly in the same temperature window, indicating a loss of positional correlation within the plane of the alkyl chains. Upon cooling, the packing of the alkyl chains is restored. We propose that during the first heating cycle the MEPE chains adopt a more condensed packing arrangement, thus reducing the layer spacing and the smoothness of the topmost interface. At temperatures above 55 °C, the integrated intensity of the Bragg peak at $q_z = 0.126$ Å^{-1} changes less rapidly and a new broad peak appears at $q_z = 0.136 \pm 5 \times 10^{-3}$ Å^{-1}, which corresponds to a spacing of $d = 46 \pm 2$ Å. In addition, the Kiessig fringes disappear completely. The increased peak width indicates a loss of out-of-plane correlation of adjacent layers (vide supra). As mentioned above, the in-plane order is also lost in this temperature range, as indicated by the absence of in-plane diffraction peaks. We note that this phase transition is irreversible.

Additionally, the temperature-dependent average Fe−N bond distance $\langle r \rangle$ determined from EXAFS measurements is plotted in Figure 4. The average Fe−N bond distance increases upon heating from 1.91 Å at room temperature to 1.95 Å at 55 °C and remains approximately constant upon further heating. The EXAFS measurements indicate that on average the coordination octahedron is elongated along the long axis of the MEPE backbone. We note that the integral character of this method averages over all distances in the sample including elongated and not elongated octahedrons. The Debye−Waller factors remain constant throughout the observed temperature range.

The kinetics of the phase transitions is studied by time- and temperature-dependent X-ray reflectivity and GID measurements. Spectra are recorded as a function of temperature with a time resolution of about 60 s. According to the Arrhenius law, a plot of the logarithm of the normalized intensities versus $1/T$ of both phase transitions yields the corresponding activation energies.[25] For the in-plane diffraction peak (Figure 4, black trace), which is associated with the alkyl chain packing, we find an activation energy for the phase transition E of 1.3 ± 0.2 eV. This energy is related to overcoming the van der Waals interactions between one particular molecule and its neighborhood.[26] With the molecular mass of one MEPE repeat unit and six DHP chains, this corresponds to a transition enthalpy of $H = 32.3 \pm 4.8$ J·g^{-1}.[27] As mentioned above, we also observe a change in the Bragg peak, which is associated to the vertical structure of the LB multilayer. This phase transition can be divided into two separate processes. The first, fast process, within the temperature range from room temperature to 55 °C, is characterized by an activation energy of $E = 1.2 \pm 0.3$ eV ($H = 29 \pm 4.8$ J·g^{-1}). The second, slower process, which starts at 55 °C, is characterized by an activation energy of $E = 0.7 \pm 0.1$ eV ($H = 17.4 \pm 2.5$ J·g^{-1}).

Summary. Here, we present a detailed analysis of the three-dimensional structure of a PAC multilayer. As shown by X-ray reflectometry, the multilayer architecture consists of alternating strata of DHP molecules and MEPE strands. A detailed analysis of the reflectance curves indicates that the phosphate headgroups are pointing toward the MEPE chains. The alkyl chains of DHP are fully extended and are oriented along the surface normal. Such a structure is in agreement with the architecture of the corresponding Langmuir monolayer at the air−water interface.[20] The overall structure corresponds to a classical Y-type architecture. The vertical correlation of adjacent strata extends up to approximately 12 transferred monolayers.

Using grazing incidence diffraction, we probe the in-plane structure of the multilayer. In agreement with the structure determined by reflectometry, the fully extended alkyl chains are packed in a hexagonal arrangement. The positional correlation extends to approximately 18 neighbors. Energy-dispersive detection also detects the K-fluorescence peak of the central Fe atoms of MEPE.

The local order around the Fe centers is determined with EXAFS. As expected, the metal ion is in an pseudo-octahedral coordination environment. The central and terminal Fe−N bond distances of 1.821 and 1.999 Å are within the experimental error in good agreement with values found in the crystal structures of mononuclear Fe bis-terpyridine complexes.[24]

The multilayer shows a reversible phase transition in the temperature range from room temperature up to 55 °C. First, the lateral ordering of the alkyl chains is lost, and second, the vertical layering and smoothening of the multilayer is reduced upon heating. A slightly reduced layer spacing upon cooling is associated with a more condensed packing arrangement of the MEPE chains. As indicated by EXAFS, the average Fe−N bond distances increase from 1.91 to 1.95 Å in the same temperature range. Both phase transitions show Arrhenius-like behavior. The estimated transition enthalpies of $H = 32.3 \pm 4.8$ J·g^{-1} and $H = 29 \pm 4.8$ J·g^{-1} correspond to values found in the bulk material. These values are typical for chain melting and interlayer diffusion in Langmuir−Blodgett multilayers.[28]

It is interesting to note that the Debye−Waller factors remain constant through the phase transition. Generally, spin transitions are accompanied by an increase in the Debye−Waller factors. The large entropy gain associated with the spin transition is

considered as a main driving force. Currently, we cannot unambiguously determine the origin of the magnetic phase transition in these metallo-supramolecular materials. It is possible that the entropy gain drives the phase transition like in so many other spin transition compounds. Alternatively, the phase transition of the matrix may cause steric strain, which gives rise to a distortion of the coordination geometry of the embedded MEPE. Any distortion of the trp−Fe geometry will lower the ligand field splitting, opening the way for a spin transition. Further experiments shall elucidate this point in more detail.

References and Notes

(1) Schubert, U. S.; Eschbaumer, C. *Angew. Chem., Int. Ed.* **2002**, *41*, 2892.

(2) Constable, E. C. *Electronic Materials: The oligomer approach*; VCH Wiley: Weinheim, Germany, 1998.

(3) Bazai, V.; Seandola, F. *Supramolecular photochemistry*; Harwood: New York, 1991.

(4) Long, N. J. *Angew. Chem., Int. Ed.* **1995**, *34*, 21.

(5) Balzani, V.; Scandola, F. *Supramolecular Photochemistry*; Ellis Horwood: New York, 1991.

(6) Decurtins, S.; Gütlich, P.; Köhler, C. P.; Spiering, H.; Hauser, A. *Chem. Phys. Lett.* **1984**, *105*, 1.

(7) Decurtins, S.; Gütlich, P.; Hasselbach, K. M.; Hauser, A.; Spiering, H. *Inorg. Chem.* **1985**, *24*, 2174.

(8) Renz, F.; Oshio, H.; Ksenofontov, H.; Waldeck, M.; Spiering, M.; Gütlich, P.; *Angew. Chem., Int. Ed.* **2000**, *39*, 3699.

(9) Kurth, D. G.; Severin, N.; Rabe, J. P. *Angew. Chem.* **2002**, *41*, 3833−3835; *Angew. Chem., Int. Ed.* **2002**, *114*, 3681−3683.

(10) (a) Meister, A.; Förster, G.; Thünemann, A.; Kurth, D. G. *ChemPhysChem* **2003**, *4*, 1095−1100. (b) Kurth, D. G.; Meister, A.; Thünemann, A.; Förster, G. *Langmuir* **2003**, *19*, 4055−4057.

(11) Bodenthin, Y.; Pietsch, U.; Möhwald, H.; Kurth, D. G. *J. Am. Chem. Soc.* **2005**, *127*, 3110.

(12) Schütte, M.; Kurth, D. G.; Linford, M. R.; Cölfen, H.; Möhwald, H. *Angew. Chem., Int. Ed.* **1998**, *37*, 2891−2893.

(13) Kurth, D. G.; Lehmann, P.; Schütte, M. *Proc. Natl. Acad. Sci. U.S.A.* **2000**, *97*, 5704−5707.

(14) Kern, W. *Semicond. Int.* **1984**, 94.

(15) Parrat, L. G. *Phys. Rev.* **1954**, *95*, 359.

(16) Bodenthin, Y.; Grenzer, J.; Lauter, R.; Pietsch, U.; Lehmann, P.; Kurth, D. G.; Möhwald, H. *J. Synchrotron Radiat.* **2002**, *9*, 206−209.

(17) Erko, A.; Packe, I.; Gudat, W.; Abrosimov, N.; Firsov, A. *SPIE* **2000**, *4145*, 122−128.

(18) Michalowicz, A.; Vlaic, G. *J. Synchrotron Radiat.* **1998**, *5*, 1317−1320.

(19) Pietsch, U.; Barberka, T. A.; Englisch, U.; Stömmer, R. *Thin Solid Films* **1996**, *284−285*, 387−391.

(20) Lehmann, P.; Kurth, D. G.; Brezesinski, G.; Symietz, Ch. *Chem.−Eur. J.* **2001**, *7*, 1646−1651.

(21) The number of coherent scattering 2D unit cells can be estimated by the Scherrer equation $L_{in} = 0.94\lambda/(2\theta_{in} \cos \theta_{in})$ where θ_{in} is given in radians as $2\theta_{in} = 2(\theta_{exp}^2 - \theta_{app}^2)^{0.5}$. θ_{app} describes the apparatus function and can be estimated as 0.75°. For an extensive treatment of the subject, see: Baberka, Th.; et al. *Thin Solid Films* **1994**, *244*, 1061−1066.

(22) Mahler, W.; Barberka, T. A.; Pietsch, U.; Höhne, U.; Merle, h. J. *Thin Solid Films* **1995**, *256*, 198−204.

(23) Thompson, A.; Vaughan, D. X-ray Data Booklet, http://xdb.lbl.gov.

(24) Baker, A. T.; Goodwin, H. A. *Aust. J. Chem.* **1985**, *38*, 207. Constable, E. C.; et al. *Chem−Eur. J.* **1999**, *5* (2), 498.

(25) Englisch, U.; Penacorada, F.; Samoilenko, I.; Pietsch, U. *Physica B* **1998**, 258−262.

(26) Salem, L. *J. Chem. Phys.* **1962**, *37*, 2100.

(27) Differential scanning calorimetry of the bulk material yields an enthalpy of 31.7 J·g^{-1}.

(28) Englisch, U.; Katholy, S.; Penacorada, F.; Reiche, J.; Pietsch, U. *Mater. Sci. Eng., C* **1999**, 8−9, 99−102.